

Symmetry-breaking instability of leapfrogging vortex rings in a Bose-Einstein condensate

Mayumi Ikuta,¹ Yumi Sugano,¹ and Hiroki Saito¹

¹*Department of Engineering Science, University of Electro-Communications, Tokyo 182-8585, Japan*

(Dated: February 5, 2019)

Three coaxial quantized vortex rings in a Bose-Einstein condensate exhibit aperiodic leapfrogging dynamics. It is found that such circular vortex rings are dynamically unstable against deformation breaking axial rotational symmetry. The dynamics of the system are analyzed using the Gross-Pitaevskii and vortex-filament models. The dependence of the instability on the initial arrangement of the vortex rings is investigated. The system is found to be significantly unstable for a specific configuration of the three vortex rings.

I. INTRODUCTION

A vortex ring has a toroidal vorticity distribution with a torus shape, and survives for a long time after it is created. A vortex ring has a linear momentum and can therefore travel a long distance, as for the well-known example of smoke rings in air. However, in a normal fluid with viscosity, such as air or water, a vortex ring eventually decays due to the dissipation of energy and momentum. Furthermore, the toroidal vorticity distribution has an inherent instability against azimuthal-wave excitation [1, 2].

In superfluids, the situation is much simpler. Vortices are quantized, and a vortex ring is simply a circular closed loop of a quantized vortex line. Because of the absence of viscosity, a circular quantized vortex ring has an infinite lifetime in a uniform superfluid. Quantized vortex rings were first detected in superfluid helium using ion spectroscopy [3]. In Bose-Einstein condensates (BECs) of ultracold atomic gases, quantized vortex rings have been created through the decay of solitons and directly observed by imaging the density distribution [4–7]. The dynamics of quantized vortex rings in superfluids have been theoretically studied by many researchers [8–24].

A circular vortex ring in a superfluid travels at a constant velocity roughly proportional to the inverse of its radius. Such a quantized vortex ring traveling in a uniform superfluid is stationary in the moving frame of reference, and stable against perturbations. When two circular vortex rings with the same vorticity are arranged in parallel sharing the same axis, the radius of the front (rear) ring increases (decreases) and the ring decelerates (accelerates). The rear ring thus passes through the front ring, and then the roles of the two rings are reversed, which results in leapfrogging dynamics of the two vortex rings [25, 26]. For more than two coaxial vortex rings, the leapfrogging dynamics become more complicated.

In the present paper, we focus on the axial-symmetry breaking instability of leapfrogging vortex rings in superfluids. When circular vortex rings are coaxially arranged in the initial state, the system has rotational symmetry about the axis of the rings. In the ensuing leapfrogging dynamics, the axial symmetry is spontaneously broken, i.e., infinitesimal azimuthal perturba-

tions are exponentially increased, and the leapfrogging dynamics are eventually destroyed by significant distortions of the rings. Such instabilities of coaxial vortex rings have been studied using the vortex-filament model. In Ref. [16], the dynamics of leapfrogging vortex rings were numerically studied and axial-symmetry breaking instability was shown to occur for seven vortex rings. A linear stability analysis was performed for two vortex rings by Ref. [20]. The long-time stability of two and three vortex rings was studied by Ref. [23].

In the present paper, we investigate the axial-symmetry breaking instability of three quantized vortex rings using both the Gross-Pitaevskii (GP) equation and the vortex-filament model. Three vortex rings with the same direction of vorticity are coaxially arranged, which exhibit leapfrogging dynamics. We find that the system is significantly unstable against axial-symmetry breaking for a specific initial arrangement of the vortex rings. The instability occurs both for the GP and vortex-filament models. We investigate the dependence of the instability on the initial arrangements of the vortex rings and on the interaction coefficient. We will show that the symmetry-breaking modulation significantly grows when the vortex rings form a particular configuration during the dynamics, and most unstable eigenmode is obtained.

This paper is organized as follows. Section II presents a study of the dynamics of vortex rings by solving the GP equation numerically. Section III analyzes the symmetry-breaking instability using the vortex-filament model. Section IV gives the conclusions of this study.

II. GROSS-PITAEVSKII MODEL

We consider a BEC of a dilute atomic gas at zero temperature described by the GP equation,

$$i\hbar\frac{\partial\psi}{\partial t} = -\frac{\hbar^2}{2M}\nabla^2\psi + V(\mathbf{r})\psi + \frac{4\pi\hbar^2 a}{M}|\psi|^2\psi, \quad (1)$$

where $\psi(\mathbf{r}, t)$ is the macroscopic wave function of the condensate, M is the mass of an atom, $V(\mathbf{r})$ is an external potential, and a is the s -wave scattering length. We normalize the length, time, energy, and atomic density by an arbitrary length L , arbitrary time T , \hbar/T , and arbitrary

density n_0 , respectively, where $\hbar T = ML^2$ is satisfied. The GP equation then becomes non-dimensional as

$$i \frac{\partial \psi}{\partial t} = -\frac{\nabla^2}{2} \psi + V(\mathbf{r})\psi + g|\psi|^2\psi, \quad (2)$$

where the non-dimensional interaction coefficient is $g = 4\pi aL^2 n_0$. To reduce the effect of boundary conditions on the axial symmetry of the vortex rings, we use a cylindrical tube potential given by

$$V(\mathbf{r}) = \begin{cases} 0 & (r_\perp < R_{\text{wall}}) \\ V_0 & (r_\perp \geq R_{\text{wall}}) \end{cases}, \quad (3)$$

where $r_\perp = (x^2 + y^2)^{1/2}$ and R_{wall} is the radius of the cylindrical tube. Such a potential can be produced by a phase-imprinted laser beam [27]. The height V_0 of the potential wall is taken to be much larger than the chemical potential $g|\psi|^2$. A periodic boundary condition is imposed in the z direction.

The initial state is prepared by the imaginary-time propagation of Eq. (2), where i on the left-hand side is replaced with -1 . The wave function is normalized with the volume of the cylindrical tube as

$$\int |\psi|^2 d\mathbf{r} = \pi R_{\text{wall}}^2 L_z, \quad (4)$$

where L_z is the size of the system in the z direction. The density $|\psi|^2$ is thus almost unity inside the tube potential, when the radius R_{wall} is much larger than the healing length. After the imaginary-time propagation converges, circular vortex rings are imprinted in such a way that their symmetry axis is on the z axis. The wave function is multiplied by $\exp[i\phi(\mathbf{r})]$, with the phase given by

$$\phi(\mathbf{r}) = \sum_{j=1}^{N_{\text{ring}}} \sum_{n=-n_z}^{n_z} \left(\tan^{-1} \frac{z - Z_j - nL_z}{r_\perp + R_j} - \tan^{-1} \frac{z - Z_j - nL_z}{r_\perp - R_j} \right), \quad (5)$$

where N_{ring} is the number of vortex rings and R_j and Z_j are the radius and z coordinate of the j th vortex ring, respectively. The first and second terms in the bracket in Eq. (5) cancel the radial flow $\partial\phi/\partial r_\perp$ on the z axis, and the summation over integers n in Eq. (5) ensures a periodic boundary condition in the z direction for a sufficiently large n_z , which reduces the initial disturbances due to the phase imprint. To further reduce the initial disturbances, we perform a short imaginary-time evolution during T_{imag} after the phase $\phi(\mathbf{r})$ is imprinted on the wave function. This imaginary-time evolution slightly changes the radii and z positions of the vortex rings from R_j and Z_j in Eq. (5).

We obtain the imaginary and real time evolution of the system by numerically solving Eq. (2) using the pseudospectral method [28]. The numerical mesh is typically 512^3 with a spatial discretization of $dx = dy = dz = 0.25$, and the system size is $L_x \times L_y \times L_z = 128^3$. Small noise

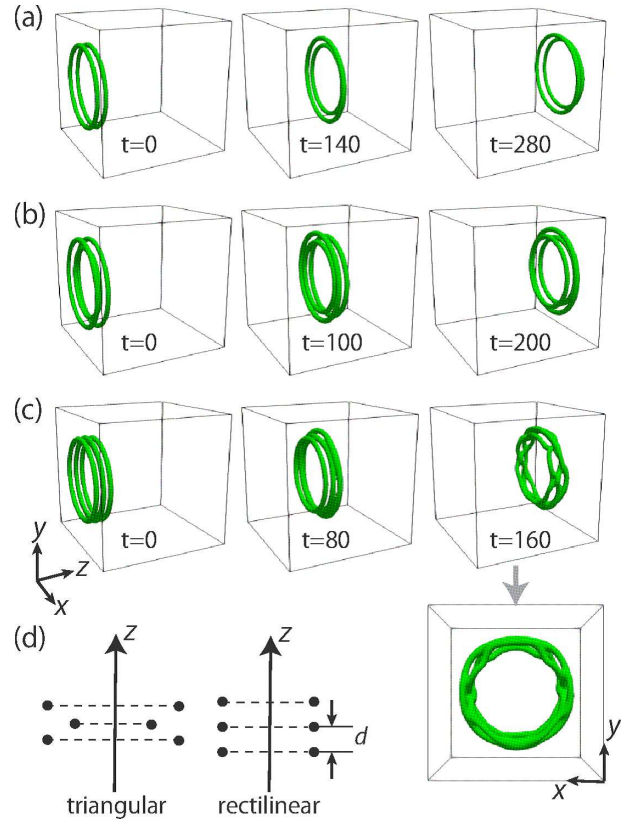


FIG. 1. (color online) (a)-(c) Dynamics of vortex rings obtained by solving the GP equation with $g = 1$. The isodensity surface of the density $|\psi|^2 = 0.5$ is shown. (a) Two vortex rings initially located with $R_1 = R_2 = 20$, $Z_1 = -28$, and $Z_2 = -26$. (b) Three vortex rings with a triangular initial arrangement, where $R_1 = 20 - 2\sqrt{3}/3$, $R_2 = R_3 = 20 + 1/\sqrt{3}$, $Z_1 = -26$, $Z_2 = -28$, and $Z_3 = -24$. (c) Three vortex rings with a rectilinear initial arrangement, where $R_1 = R_2 = R_3 = 20$, $Z_1 = -27$, $Z_2 = -26$, and $Z_3 = -28$. The vortices seen from the $+z$ direction at $t = 160$ are highlighted. Axial symmetry is retained in (a) and (b) and broken in (c) in the time evolution. The size of the box is 64^3 , with the origin at the center. See the Supplemental Material for movies showing the dynamics [29]. (d) Initial vortex arrangements set by Eq. (5). The triangular and rectilinear arrangements used in (b) and (c) are shown in the left-hand and right-hand panels, respectively, where the dots represent the positions of vortex cores on the plane including the z axis.

must be added to the initial state to trigger the symmetry breaking instability. To generate moderate noise, we first set complex random numbers with a normal distribution on each numerical mesh point and eliminate large wavenumber components with $k > k_{\text{cutoff}}$ using a Fourier transform, where k_{cutoff} is taken to be $10 \times 2\pi/128$. Such low-pass filtered noise multiplied by a small number (typically 0.1) is added to the wave function after the imaginary-time evolution for T_{imag} . In the following calculations, we take $V_0 = 10$, $R_{\text{wall}} = 63$, $n_z = 50$, and $T_{\text{imag}} = 4$.

Figure 1 shows the time evolution of two and three vor-

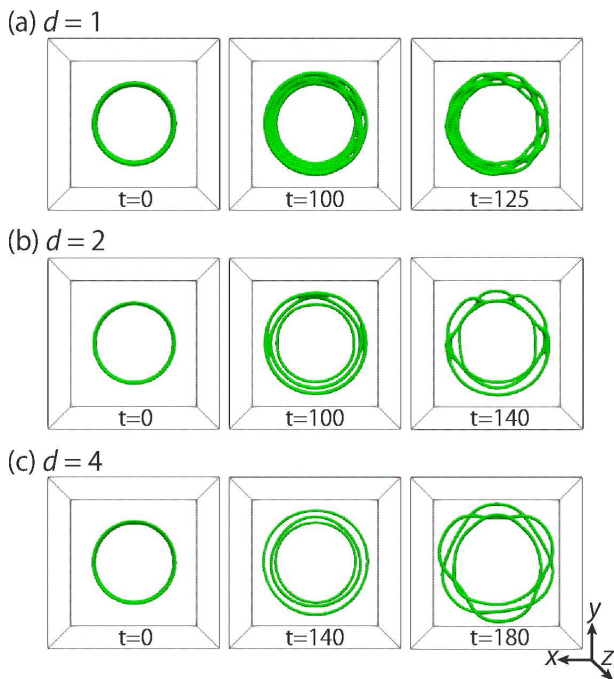


FIG. 2. (color online) Dependence of the symmetry breaking dynamics on the initial distance d between the vortex rings in the rectilinear initial arrangement with radius $R = 20$. The dynamics are obtained by solving the GP equation with $g = 1$. (a) $d = 1$, (b) $d = 2$, and (c) $d = 4$. The dynamics in (b) is the same as that in Fig. 1(c). The isodensity surface of the density $|\psi|^2 = 0.2$ is shown. The size of the box is 64^3 , with the origin at the center, and is seen from the $+z$ direction. See the Supplemental Material for movies showing the dynamics [29].

tex rings (see the Supplemental Material for movies [29]). Figure 1(a) shows the case of two vortex rings that are coaxially arranged at $t = 0$. They exhibit periodic leapfrogging dynamics and travel in the $+z$ direction, in which the axial symmetry is retained. Figure 1(b) shows the case of three vortex rings coaxially arranged so that the six vortex cores form two regular triangles on the plane including the symmetry axis, as illustrated in the left-hand panel in Fig. 1(d). We refer to such an initial arrangement of vortex rings as a “triangular” arrangement. The rings in this arrangement also exhibit periodic leapfrogging dynamics such that the triangles of the vortex cores rotate around their centers. The axial symmetry is retained for a long time in the leapfrogging dynamics for the triangular configuration, as reported for the vortex-filament model [16, 23]. We have numerically confirmed that the axially-symmetric leapfrogging dynamics continue at least until $t \simeq 500$ for Figs. 1(a) and 1(b).

In Fig. 1(c), three vortex rings with the same radius are coaxially and equidistantly arranged along the z axis. We refer to such an initial arrangement as a “rectilinear” arrangement. The leapfrogging dynamics is irregular for this initial state. We label the vortex rings A, B, and C

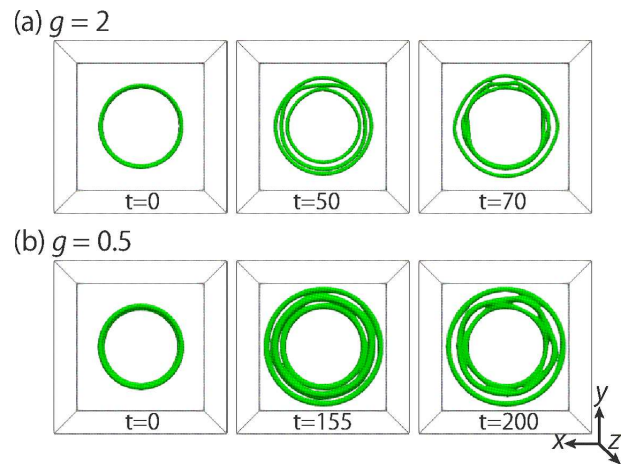


FIG. 3. (color online) Dependence of symmetry-breaking dynamics on interaction coefficient g for vortex rings in rectilinear initial arrangement with $d = 2$ and $R = 20$. The dynamics are obtained by solving the GP equation. (a) $g = 2$ and (b) $g = 0.5$. The isodensity surfaces of the densities $|\psi|^2 = 0.5$ and 0.2 are shown for (a) and (b), respectively. The size of the box is 64^3 with the origin at the center, and is seen from the $+z$ direction. See the Supplemental Material for movies showing the dynamics [29].

from front to rear in the initial arrangement. First, B and C pass through A, and the order is reversed as C, B, A from front to rear. Then A and B pass through C, during which a leapfrog occurs between A and B, resulting in the order B, A, C from front to rear. Next, A is overtaken by C, which gives the snapshot at $t = 80$ in Fig. 1(c). We can see that the axial symmetry starts to break at this time. Subsequently, the axial symmetry breaking develops as irregular leapfrogging dynamics. The vortex lines then intertwine with each other and reconnections occur.

Figure 2 shows the dynamics seen from the $+z$ direction for the rectilinear initial arrangement with various distances d between the vortex rings. We see that the axial symmetry is broken at $t \sim 100$, and the unstable modes depend on the initial distance d . The wavelengths of the unstable modes are $\simeq 2\pi R/8$ in Fig. 2(a), $\simeq 2\pi R/4$ in Fig. 2(b), and $\simeq 2\pi R/3$ in Fig. 2(c) with R being the radius of the vortex ring, which indicates that the most unstable wavelength increases with d . The growth rate for the unstable mode tends to decrease with increasing d . The distances indicated in Fig. 2 are the distances between the vortex rings in the phase imprint by Eq. (5). By the imaginary-time evolution for $T_{\text{imag}} = 4$ after the phase imprint, the distance between adjacent vortices changes from $d = 1, 2$, and 4 to $d \simeq 2, 3.5$, and 5 , respectively.

Figure 3 shows the dependence of the symmetry-breaking dynamics on the interaction coefficient g . For $g = 2$, the wavelength of the unstable mode is $\simeq 2\pi R/4$ (or $\simeq 2\pi R/3$), as shown in Fig. 3(a). For $g = 0.5$, the unstable wavelength is $\simeq 2\pi R/5$, as shown in

Fig. 3(b). This difference is purely due to the difference in g , because the distance d between the vortices after the imaginary-time propagation is almost the same for Figs. 3(a) and 3(b). For a larger value of g , the healing length becomes smaller, and therefore, the spatial discretization dx , dy , and dz must be decreased and the numerical mesh must be increased. For a smaller value of g , the time for which the instability emerges increases and long-time evolution is needed.

The symmetry-breaking instability demonstrated in Figs. 1-3 is a modulational instability (or dynamical instability), in which infinitesimal symmetry-breaking noise grows exponentially with time. However, in the present case, the standard linear stability analysis, i.e., Bogoliubov analysis, cannot be used, since the vortex rings move and the system is not in a stationary state. We also cannot use the Floquet analysis, since the dynamics of the three vortex rings are not periodic for the rectilinear initial arrangement.

III. VORTEX-FILAMENT MODEL

To study the symmetry-breaking dynamics of vortex rings in more detail, we employ the vortex-filament model. In this model, we focus only on the dynamics of quantized vortex lines. We assume that the fluid is incompressible and irrotational except at the vortex lines. A vortex segment located at \mathbf{r} moves with the velocity given by the Biot-Savart law,

$$\mathbf{v}(\mathbf{r}) = \frac{\kappa}{4\pi} \int \frac{(\mathbf{r}' - \mathbf{r}) \times d\mathbf{r}'}{|\mathbf{r} - \mathbf{r}'|^3}, \quad (6)$$

where $\kappa = 2\pi$ is the normalized circulation of a quantized vortex and the line integral is taken along all vortex lines.

In the numerical calculations, the n th vortex ring is represented by a sequence of N_p positions on the ring, $\mathbf{S}_1^{(n)}$, $\mathbf{S}_2^{(n)}$, \dots , $\mathbf{S}_{N_p}^{(n)}$, and $\mathbf{S}_{N_p+1}^{(n)} = \mathbf{S}_1^{(n)}$. The Biot-Savart integral in Eq. (6) is then rewritten as

$$\begin{aligned} \mathbf{v}(\mathbf{r}) &= \frac{\kappa}{4\pi} \sum_{n=1}^{N_{\text{ring}}} \sum_{j=1}^{N_p} \int_{\mathbf{S}_j^{(n)}}^{\mathbf{S}_{j+1}^{(n)}} \frac{(\mathbf{r}' - \mathbf{r}) \times d\mathbf{r}'}{|\mathbf{r} - \mathbf{r}'|^3} \\ &\equiv \frac{\kappa}{4\pi} \sum_{n=1}^{N_{\text{ring}}} \sum_{j=1}^{N_p} F_j^{(n)}(\mathbf{r}). \end{aligned} \quad (7)$$

We approximate the vortex line between $\mathbf{S}_j^{(n)}$ and $\mathbf{S}_{j+1}^{(n)}$ to be a straight line [30, 31], and the line integral becomes

$$F_j^{(n)}(\mathbf{r}) = \frac{(D_j^{(n)} + D_{j+1}^{(n)})(\mathbf{D}_j^{(n)} \times \mathbf{D}_{j+1}^{(n)})}{D_j^{(n)} D_{j+1}^{(n)} (D_j^{(n)} D_{j+1}^{(n)} + \mathbf{D}_j^{(n)} \cdot \mathbf{D}_{j+1}^{(n)}), \quad (8)$$

where $\mathbf{D}_j^{(n)} = \mathbf{S}_j^{(n)} - \mathbf{r}$. Since the vortex-filament model breaks down for $|\mathbf{r} - \mathbf{r}'|$ smaller than the size of the vortex core ξ , we omit the line integral inside the vortex core, $|\mathbf{r}' - \mathbf{r}| < \xi$, in Eqs. (7) and (8), which avoids the

divergence at $\mathbf{r}' = \mathbf{r}$. The length ξ corresponds to the healing length in the GP model and we take $\xi = 1$, corresponding to $g = 1$. The number of points per vortex ring is taken to be $N_{\text{ring}} = 256$. Because the radii of the rings that we are considering are $\simeq 20$, the distance between the adjacent points $|\mathbf{S}_j^{(n)} - \mathbf{S}_{j+1}^{(n)}|$ is typically $2\pi \times 20/256 \simeq 0.5 \lesssim \xi$. This is in contrast to the case of liquid helium [30], in which the size of the vortex core is $\sim 10^{-10}$ m and usually much smaller than the distance between the adjacent points $|\mathbf{S}_j^{(n)} - \mathbf{S}_{j+1}^{(n)}|$. We do not implement vortex reconstructions in our calculations, because we focus on the axial-symmetry breaking.

The dynamics of $N_{\text{ring}} \times N_p$ points are obtained by numerically solving the equation of motion $d\mathbf{S}_j^{(n)}/dt = \mathbf{v}(\mathbf{S}_j^{(n)})$ using the fourth-order Runge-Kutta method. The initial positions of the points are set to

$$\mathbf{S}_j^{(n)} = R_n \mathbf{r}_j + Z_n \mathbf{z}, \quad (9)$$

where R_n and Z_n are the radius and z -coordinate of the n th vortex ring, $\mathbf{r}_j = \mathbf{x} \cos(2\pi j/N_p) + \mathbf{y} \sin(2\pi j/N_p)$ is the unit vector in the radial direction, and \mathbf{x} , \mathbf{y} , and \mathbf{z} are the unit vectors in Cartesian coordinate. Small initial noise is added to each point to trigger the axial symmetry breaking. To avoid numerical instability in the vortex-filament model, we cut off the large wavenumber components in each time step as follows. We perform a Fourier transform of the radius and z -coordinate as

$$c_m^{(n)} = \sum_{j=1}^{N_p} \sqrt{(\mathbf{S}_j^{(n)} \cdot \mathbf{x})^2 + (\mathbf{S}_j^{(n)} \cdot \mathbf{y})^2} e^{-imj}, \quad (10)$$

$$d_m^{(n)} = \sum_{j=1}^{N_p} \mathbf{S}_j^{(n)} \cdot \mathbf{z} e^{-imj}, \quad (11)$$

where m is an integer and $c_{-m}^{(n)} = c_m^{(n)*}$ and $d_{-m}^{(n)} = d_m^{(n)*}$ are satisfied. We then eliminate Fourier components with $|m|$ larger than m_{cutoff} , and perform an inverse Fourier transform as

$$\mathbf{S}_j^{(n)} = N_p^{-1} \sum_{|m| \leq m_{\text{cutoff}}} (c_m^{(n)} \mathbf{r}_j + d_m^{(n)} \mathbf{z}) e^{imj}. \quad (12)$$

We take $m_{\text{cutoff}} = 10$ in the following calculations.

Figure 4 shows the dynamics of vortex rings. In Fig. 4(a), two vortex rings with the same radius $R_1 = R_2 = 20$ are coaxially arranged at a distance $Z_2 - Z_1 = 4$ in the initial state, and they exhibit periodic leapfrogging dynamics in the time evolution. The frequency of the leapfrogging dynamics in Fig. 4(a) is similar to that in the GP model in Fig. 1(a). The period of the leapfrogging dynamics is roughly proportional to the distance between the vortex rings. In the GP model in Fig. 1(a), the distance is $Z_2 - Z_1 = 2$ in the initial phase imprint, though this increases during the imaginary-time evolution for T_{imag} , which is why the leapfrog frequency in Fig. 1(a) is similar to that in Fig. 4(a) with the initial

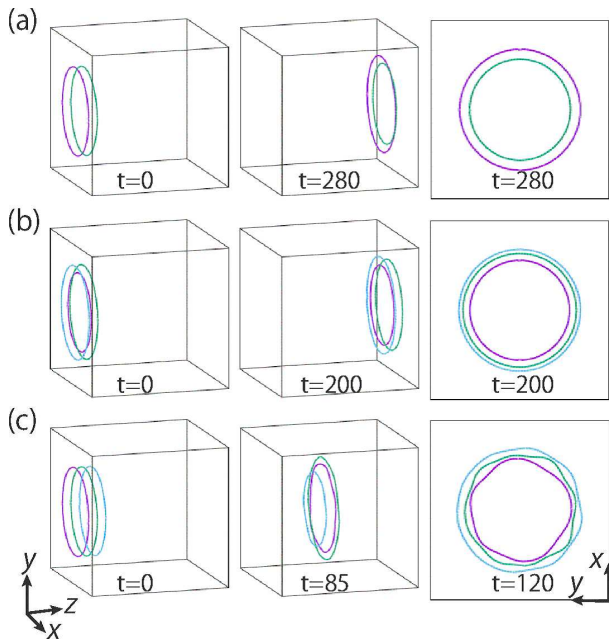


FIG. 4. (color online) Dynamics of vortex rings obtained by the vortex-filament model. (a) Two vortex rings initially located with $R_1 = R_2 = 20$, $Z_1 = -30$, and $Z_2 = -26$. (b) Three vortex rings with a triangular initial arrangement, where $R_1 = 20 - 4\sqrt{3}/3$, $R_2 = R_3 = 20 + 2/\sqrt{3}$, $Z_1 = -28$, $Z_2 = -26$, and $Z_3 = -30$. (c) Three vortex rings with a rectilinear initial arrangement, where $R_1 = R_2 = R_3 = 20$, $Z_1 = -30$, $Z_2 = -26$, and $Z_3 = -22$. Vortices are seen from the $+z$ direction in the rightmost panels. Axial symmetry is retained in (a) and (b) and broken in (c). The size of the box is 64^3 with the origin at the center. See the Supplemental Material for movies showing the dynamics [29].

distance $Z_2 - Z_1 = 4$. The vortex-core structure in the GP model may also affect the leapfrog frequency, which is not included in the vortex-filament model.

Figures 4(b) and 4(c) show the dynamics of three vortex rings with triangular and rectilinear initial arrangements, respectively. For the triangular initial arrangement, the three vortex rings exhibit almost periodic leapfrogging dynamics and the axial symmetry is retained until $t = 200$, as shown in Fig. 4(b). For the rectilinear initial arrangement, in contrast, the axial symmetry is broken and modulation arises after a few leapfrogs, as shown in Fig. 4(c). This behavior of the vortex rings is similar to that in the GP model in Fig. 1.

The degree of axial symmetry breaking is quantified by the Fourier coefficients $c_m^{(n)}$ and $d_m^{(n)}$ in Eqs. (10) and (11) for $m \neq 0$. We define the degree of axial symmetry breaking for mode m as

$$C_m = \sum_{n=1}^{N_{\text{ring}}} (|c_m^{(n)}|^2 + |d_m^{(n)}|^2). \quad (13)$$

Figures 5(a) and 5(b) show the time evolution of C_m for the dynamics in Figs. 4(b) and 4(c), respectively. The

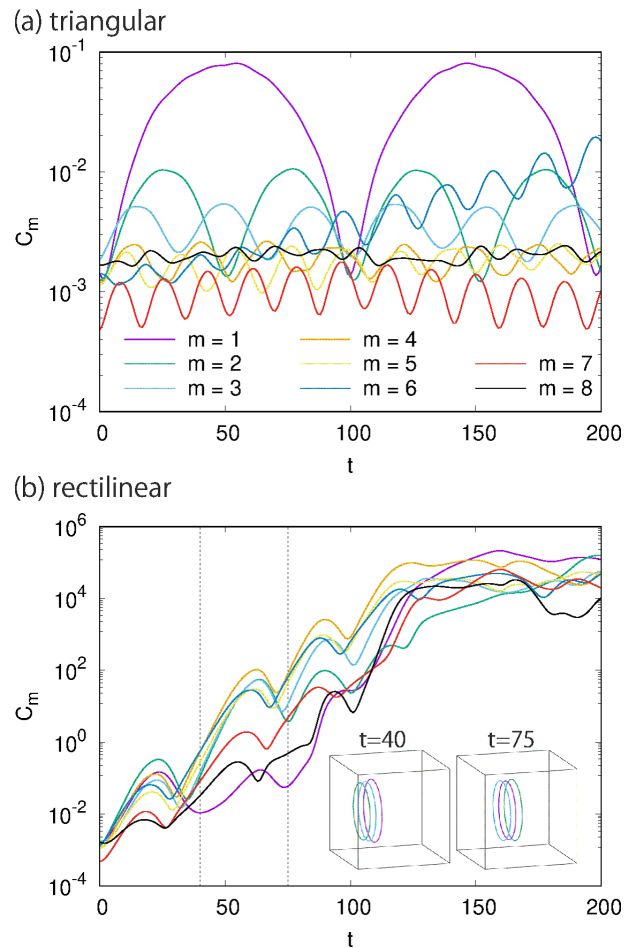


FIG. 5. (color online) Time evolution of the Fourier components C_m defined in Eq. (13). (a) and (b) correspond to the dynamics in Figs. 4(b) and 4(c), respectively. The vertical dashed lines in (b) indicate $t = 40$ and $t = 75$, for which C_m is exponentially rising. The insets in (b) show the vortex rings at these times.

initial values of $C_m \sim 10^{-3}$ originate from the initial random noise. For the triangular initial arrangement, the values of C_m are suppressed below 10^{-1} until $t = 200$, as shown in Fig. 5(a). They oscillate and never grow for $m \neq 6$. The growth of the $m = 6$ mode is slow and only affects the long-time dynamics [23]. The time evolution of C_m for the rectilinear initial arrangement in Fig. 5(b) is qualitatively different from that in Fig. 5(a). The values of C_m exponentially grow in time as they oscillate, reflecting the fact that axial symmetry breaking occurs in Fig. 4(c). The value of C_m with $m = 4$ is largest for $t \simeq 100$ in Fig. 5(b), which gives the modulation of the rings shown in Fig. 4(c).

We note that the significant growth of C_4 occurs roughly periodically, e.g., at $t \simeq 40$ and $t \simeq 75$, as indicated by the vertical dashed lines in Fig. 5(b). The vortex-ring configurations at $t = 40$ and $t = 75$ are shown as the insets in Fig. 5(b). We find that the three vortex rings align in a rectilinear manner at these instants, and

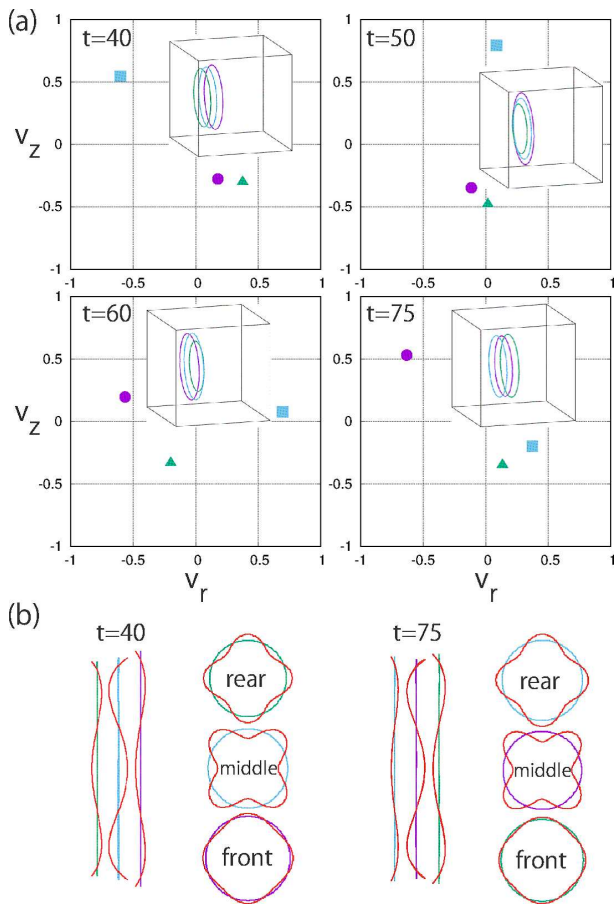


FIG. 6. (color online) The most unstable eigenvector of Eq. (14) for $m = 4$. The three vortex rings are initially in the rectilinear configuration, as in Fig. 4(c). (a) The most unstable eigenvectors, $(c_4^{(1)}, d_4^{(1)})$, $(c_4^{(2)}, d_4^{(2)})$, and $(c_4^{(3)}, d_4^{(3)})$ are plotted at each time, where the circles, triangles, and squares correspond to the vortex rings in the inset with the same colors (gray scales). (b) Shape of the most unstable mode with $m = 4$ at $t = 40$ and $t = 75$. The three vortex rings are seen from the $+x$ direction in the left-hand panel at each time. In the right-hand panels, the three vortex rings seen from the $+z$ direction are separately shown for clarity.

the two vortex rings in the back are about to pass through the front vortex ring. Figure 5(b) indicates that such dynamics significantly increase the symmetry-breaking modulation of the vortex rings. For the triangular initial arrangement, on the other hand, such a rectilinear configuration of the three vortex rings is not realized in the time evolution, and hence C_m does not grow significantly. The physical explanation for why such a vortex configuration is unstable has yet to be clarified.

To study the unstable modes, we perform a linear stability analysis. The symmetry-breaking modulation of the m th mode is represented by the Fourier coefficients in Eqs. (10) and (11), which we write as a vector $\mathbf{v}_m = (c_m^{(1)}, d_m^{(1)}, c_m^{(2)}, d_m^{(2)}, c_m^{(3)}, d_m^{(3)})^T$, with T being the transpose. When the modulation is small, we can lin-

earize the equation of motion with respect to \mathbf{v}_m , and therefore, we can linearize the time evolution of the modulation as

$$\mathbf{v}_m(t) = M(t)\mathbf{v}_m(0), \quad (14)$$

where $M(t)$ is a 6×6 matrix. The modes with different m are not coupled with each other [1]. We obtain the matrix $M(t)$ numerically as follows. First, we set the initial vector as $\mathbf{v}_m(0) = (\epsilon, 0, 0, 0, 0, 0)^T$ and make the initial vortex rings using Eq. (12), where $\epsilon \ll 1$. After the time evolution of the vortex rings, $\mathbf{v}_m(t)$ is obtained with Eqs. (10) and (11), which gives $(M_{11}(t), M_{21}(t), \dots, M_{61}(t))^T = \mathbf{v}_m(t)/\epsilon$. In a similar manner, we obtain all the matrix elements of $M(t)$.

The eigenvector of $M(t)$ with the eigenvalue having the largest magnitude corresponds to the most unstable mode. Figure 6 shows the form of the most unstable eigenvector for $m = 4$ with the triangular initial arrangement as in Fig. 4(c). All the elements of the eigenvector can be taken to be real. In Fig. 6(a), we plot the most unstable mode on the c_m - d_m plane. At $t = 40$, the square (corresponding to the middle vortex ring) is located opposite the circle and triangle (corresponding to the front and rear vortex rings) across the origin. These plots move in time as the leapfrog dynamics of the vortex rings, and at $t = 75$, the circle (corresponding to the middle vortex ring) is located opposite the triangle and square (corresponding to the front and rear vortex rings) across the origin. These eigenvectors of the unstable mode are visualized in Fig. 6(b), where the modulation is superimposed on the unmodulated vortex rings in an exaggerated manner. We find that the modes at $t = 40$ and $t = 75$ have similar shapes, despite the order of the vortex rings changing. At both $t = 40$ and $t = 75$, the deviations from the unperturbed vortex rings in adjacent vortex rings are opposite to each other.

Figure 7 shows the dependence of the axial symmetry breaking on the initial distance d between the vortex rings for the rectilinear initial arrangement. In Fig. 7(a), the initial distance is $d = 6$, which is larger than $d = 4$ in Fig. 4(c). The axial symmetry breaking becomes significant at $t \simeq 300$ and the modes $m = 2$ or 3 seem to be the most unstable. For $d = 3$, as shown in Fig. 7(b), the modulation with $m \simeq 8$ becomes significant at $t \gtrsim 60$. Thus, the wavelength of the symmetry-breaking modulation increases and the growth rate of the modulation decreases with increasing d , which agrees with the tendency in the GP model shown in Fig. 2.

IV. CONCLUSIONS

We have investigated the dynamics of coaxially arranged multiple vortex rings using the GP model and vortex-filament model. In both models, three vortex rings with rectilinear initial arrangement (Fig. 1(d), right-hand panel) are found to be very unstable, and the axial rotational symmetry of the system is spontaneously

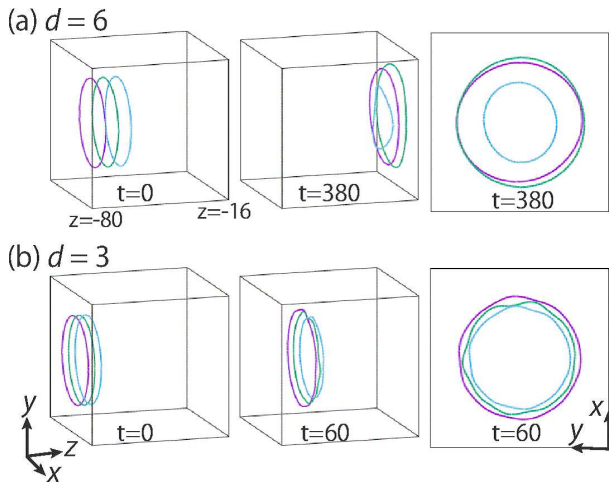


FIG. 7. (color online) Dependence of symmetry breaking dynamics on initial distance d between vortex rings for rectangular initial arrangement with radius $R = 20$. The dynamics are obtained by the vortex-filament model. (a) $d = 6$ with $Z_1 = -70$, $Z_2 = -64$, and $Z_3 = -58$. (b) $d = 3$ with $Z_1 = -30$, $Z_2 = -27$, and $Z_3 = -24$. The size of the box is 64^3 with the z axis at the center. $-80 < z < -16$ is shown at $t = 0$ in (a) and $-32 < z < 32$ is shown in the other boxes. The rightmost panels show the system seen from the $+z$ direction. See the Supplemental Material for movies showing the dynamics [29].

broken within a few leapfrogs, as shown in Figs. 1(c) and 4(c). In contrast, three vortex rings with a triangular initial arrangement (Fig. 1(d), left-hand panel) are much more stable, as shown in Figs. 1(b) and 4(b). In the GP model, we have shown that the most unstable wavelength depends on the initial distance between the vortex rings (Fig. 2) and the interaction coefficient (Fig. 3). In the vortex-filament model, we performed a Fourier analysis of the modulation of the vortex rings, and found that the symmetry-breaking modulation significantly grows when the three vortex rings are arranged in a line and the rear vortex rings are about to pass through the front ring (Fig. 5(b)). The shape of the unstable mode was obtained (Fig. 6).

Such symmetry-breaking dynamics of multiple vortex rings are difficult to observe in experiments, since coaxial vortex rings with axial rotational symmetry must be created in a controlled manner. Phase imprinting [32, 33] and dynamical [34, 35] methods may realize such an arrangement of quantized vortex rings in an atomic BEC.

ACKNOWLEDGMENTS

We thank M. Tsubota and S. Yui for their valuable comments on the vortex-filament method. This work was supported by JSPS KAKENHI Grant Numbers JP17K05595, JP17K05596, and JP16K05505.

-
- [1] S. E. Widnall and J. P. Sullivan, On the stability of vortex rings, *Proc. R. Soc. Lond. A* **332**, 335 (1973).
- [2] Y. Fukumoto and Y. Hattori, Curvature instability of a vortex ring, *J. Fluid Mech.* **279**, 351 (1994).
- [3] G. W. Rayfield and F. Reif, Quantized vortex rings in superfluid helium, *Phys. Rev.* **136**, A1194 (1964).
- [4] B. P. Anderson, P. C. Haljan, C. A. Regal, D. L. Feder, L. A. Collins, C. W. Clark, and E. A. Cornell, Watching dark solitons decay into vortex rings in a Bose-Einstein condensate, *Phys. Rev. Lett.* **86**, 2926 (2001).
- [5] N. S. Ginsberg, J. Brand, and L. V. Hau, Observation of hybrid soliton vortex-ring structures in Bose-Einstein condensates, *Phys. Rev. Lett.* **94**, 040403 (2005).
- [6] I. Shomroni, E. Lahoud, S. Levy, and J. Steinhauer, Evidence for an oscillating soliton/vortex ring by density engineering of a Bose-Einstein condensate, *Nat. Phys.* **5**, 193 (2009).
- [7] C. Becker, K. Sengstock, P. Schmelcher, P. G. Kevrekidis, and R. Carretero-González, Inelastic collisions of solitary waves in anisotropic Bose-Einstein condensates: slingshot events and expanding collision bubbles, *New J. Phys.* **15**, 113028 (2013).
- [8] J. Koplik and H. Levine, Scattering of superfluid vortex rings, *Phys. Rev. Lett.* **76**, 4745 (1996).
- [9] B. Jackson, J. F. McCann, and C. S. Adams, Vortex line and ring dynamics in trapped Bose-Einstein condensates, *Phys. Rev. A* **61**, 013604 (1999).
- [10] S. Komineas and N. Papanicolaou, Vortex rings and Lieb modes in a cylindrical Bose-Einstein condensate, *Phys. Rev. Lett.* **89**, 070402 (2002).
- [11] L.-C. Crasovan, V. M. Pérez-García, I. Danaila, D. Mihalache, and L. Torner, Three-dimensional parallel vortex rings in Bose-Einstein condensates, *Phys. Rev. A* **70**, 033605 (2004).
- [12] S. Komineas and J. Brand, Collisions of solitons and vortex rings in cylindrical Bose-Einstein condensates, *Phys. Rev. Lett.* **95**, 110401 (2005).
- [13] T.-L. Horng, S.-C. Gou, and T.-C. Lin, Bending-wave instability of a vortex ring in a trapped Bose-Einstein condensate, *Phys. Rev. A* **74**, 041603(R) (2006).
- [14] J. L. Helm, C. F. Barenghi, and A. J. Youd, Slowing down of vortex rings in Bose-Einstein condensates, *Phys. Rev. A* **83**, 045601 (2011).
- [15] M. D. Reichl and E. J. Mueller, Vortex ring dynamics in trapped Bose-Einstein condensates, *Phys. Rev. A* **88**, 053626 (2013).
- [16] D. H. Wacks, A. W. Baggaley, and C. F. Barenghi, Coherent laminar and turbulent motion of toroidal vortex bundles, *Phys. Fluids* **26**, 027102 (2014).
- [17] D. H. Wacks, A. W. Baggaley, and C. F. Barenghi, Large-scale superfluid vortex rings at nonzero temperatures, *Phys. Rev. B* **90**, 224514 (2014).
- [18] R. M. Caplan, J. D. Talley, R. Carretero-González, and P. G. Kevrekidis, Scattering and leapfrogging of vortex rings in a superfluid, *Phys. Fluids* **26**, 097101 (2014).
- [19] R. N. Bisset, W. Wang, C. Ticknor, R. Carretero-

- González, D. J. Frantzeskakis, L. A. Collins, and P. G. Kevrekidis, Bifurcation and stability of single and multiple vortex rings in three-dimensional Bose-Einstein condensates, *Phys. Rev. A* **92**, 043601 (2015).
- [20] S. S. Gubser, B. Horn, and S. Parikh, Perturbations of vortex ring pairs, *Phys. Rev. D* **93**, 046001 (2016).
- [21] T. Zhu, M. L. Evans, R. A. Brown, P. M. Walmsley, and A. I. Golov, Interactions between unidirectional quantized vortex rings, *Phys. Rev. Fluids* **1**, 044502 (2016).
- [22] W. Wang, R. N. Bisset, C. Ticknor, R. Carretero-González, D. J. Frantzeskakis, L. A. Collins, and P. G. Kevrekidis, Single and multiple vortex rings in three-dimensional Bose-Einstein condensates: Existence, stability, and dynamics, *Phys. Rev. A* **95**, 043638 (2017).
- [23] V. P. Ruban, Three-dimensional stability of leapfrogging quantum vortex rings, *Phys. Fluids* **30**, 084104 (2018).
- [24] C. Ticknor, W. Wang, and P. G. Kevrekidis, Spectral and dynamical analysis of a single vortex ring in anisotropic harmonically trapped three-dimensional Bose-Einstein condensates, *Phys. Rev. A* **98**, 033609 (2018).
- [25] H. von Helmholtz, On integrals of the hydrodynamic equations which express vortex motions, *Crelle's J.* **55**, 25 (1858) [*Philos. Mag. Ser. 4* **33**, 485 (1867)].
- [26] V. V. Meleshko, A. A. Gourjii, and T. S. Krasnopolskaya, Vortex rings: history and state of the art, *J. Math. Sci.* **187**, 772 (2012).
- [27] A. L. Gaunt, T. F. Schmidutz, I. Gotlibovych, R. P. Smith, and Z. Hadzibabic, Bose-Einstein condensation of atoms in a uniform potential, *Phys. Rev. Lett.* **110**, 200406 (2013).
- [28] W. H. Press, S. A. Teukolsky, W. T. Vetterling, and B. P. Flannery, *Numerical Recipes*, 3rd ed. (Cambridge Univ. Press, Cambridge, 2007).
- [29] See Supplemental Material at <http://link.aps.org/supplemental/...> for movies of the dynamics.
- [30] K. W. Schwarz, Three-dimensional vortex dynamics in superfluid ^4He : Line-line and line-boundary interactions, *Phys. Rev. B* **31**, 5782 (1985).
- [31] D. C. Samuels, Vortex filament methods for superfluids, in *Quantized Vortex Dynamics and Superfluid Turbulence* (Springer Verlag, Berlin 2001) edited by C. F. Barenghi, R. J. Donnelly, and W. F. Vinen.
- [32] J. Ruostekoski and J. R. Anglin, Creating vortex rings and three-dimensional skyrmions in Bose-Einstein condensates, *Phys. Rev. Lett.* **86**, 3934 (2001).
- [33] J. Ruostekoski and Z. Dutton, Engineering vortex rings and systems for controlled studies of vortex interactions in Bose-Einstein condensates, *Phys. Rev. A* **72**, 063626 (2005).
- [34] F. Pinsker and N. Berloff, Nonlinear quantum piston for the controlled generation of vortex rings and soliton trains, *Phys. Rev. A* **87**, 053624 (2013).
- [35] V. I. Yukalov, A. N. Novikov, E. P. Yukalova, and V. S. Bagnato, Vortex rings and vortex ring solitons in shaken Bose-Einstein condensate, *J. Phys. Conf. Ser.* **691** 012019 (2016).